

Design, fabrication and test of an X-band 9 MeV standing-wave electron linear accelerator

Jian Gao^{1,2}, Hao Zha^{1,2}, Jia-Ru Shi^{1,2*}, Qiang Gao^{1,2}, Xian-Cai Lin^{1,2}, Fang-Jun Hu^{1,2} & Qing-Zhu Li^{1,2},
Huai-Bi Chen^{1,2}

¹Department of Engineering Physics, Tsinghua University, Beijing 100084, China

²Key Laboratory of Particle and Radiation Imaging (Tsinghua University), Ministry of
Education, Beijing 100084, China

*Corresponding author. E-mail address: shij@mail.tsinghua.edu.cn

Author Contribution Statement

Jian Gao: Conceptualization, Methodology, Software, Writing— original draft.

Hao Zha: Conceptualization, Writing – review & editing, Supervision.

Jia-Ru Shi: Writing – review & editing, Supervision.

Qiang Gao: Writing – review & editing, Supervision.

Xian-Cai Lin: Writing – review & editing, Supervision.

Fang-Jun Hu: Writing – review & editing, Supervision.

Qing-Zhu Li: Writing – review & editing, Supervision.

Huai-Bi Chen: Writing – review & editing, Supervision.

Abstract

An X-band 9 MeV standing-wave (SW) bi-periodic linear accelerator was developed for medical radiotherapy. Electrons can be accelerated to 9 MeV with a 2.4 MW klystron. The structure works at $\pi/2$ mode and adopts magnetic coupling between cavities, generating an appropriate adjacent mode separation of 10 MHz. It is less than 600 mm long, consisting of 4 bunching cells and 29 normal cells. We have conducted geometry optimization, full-scale RF simulation, as well as beam dynamics calculation. The accelerator was fabricated and then measured in the low-power RF test. The cold test results show a good agreement between the simulation and actual measurement. In the high-power RF test, the output beam current, the energy spectrum, the capture ratio, and the spot size at the exit of the accelerator have been measured. With a 2.4 MW input power, the pulse current is 100 mA and the output spot root-mean-square (RMS) radius was about 0.5 mm. The output kinetic energy is 9.04 MeV with a spectrum FWHM of 3.5%, which demonstrates good performance of this accelerator.

Keywords: Standing-wave accelerating structure, RF analysis, thermal DC gun, low-power RF test, high-power experiment.

Introduction

Applications for the electron linear accelerator are common in both industry and medicine. They include radiotherapy, nondestructive testing, industrial irradiation, and sterilizing [1]. Currently, most electron linear accelerators are operated at S-band. The large weight and vast volume provide various difficulties during testing and installation, such as a lack of space in the operating room for intraoperative irradiation. Linear accelerators operated at C-band and X-band, have been suggested to overcome those problems [2-4].

For the past few years, the X-band electron linear accelerator attracted extensive attentions worldwide. In comparison to S-band and C-band linear accelerators, X-band linear accelerators have advantages in compact structure, less weight and relatively high accelerating gradient. The accelerator laboratory at Tsinghua University has also conducted researches in this field [5]. During the past ten years, S-band and C-band SW linear accelerators driven by domestic magnetrons have been studied successfully [6-9].

Narrow energy spread is meaningful for radiotherapy since it can significantly impact the dosage rate. For a linear accelerator, the consumption of RF power is as follows [10]:

* Corresponding author: Jia-Ru Shi (E-mail: shij@mail.tsinghua.edu.cn)

$$P_{in} = \frac{V_m^2}{R_s} + V_a I, \quad (1)$$

where V_m is the maximum kinetic energy of accelerated electrons, V_a is the average energy of accelerated electrons. For the same input power and beam current, a large energy spread leads to a decreasing V_a and increasing V_m . The energy spread will severely decline of radiation dose rate, which is unacceptable for radiotherapy. As a result, medical linear accelerators with narrow energy spread have attracted significant attentions.

With a 2.4 MW input RF power source, we have designed a compact X-band SW linear accelerator in Tsinghua University, with purpose for medical applications such as X-ray radiotherapy and intraoperative electron beam radiotherapy. The design goal is to achieve a 100 mA pulse current with the kinetic energy of 9.0 MeV. Besides, the length of the accelerating structure is less than 600 mm. We choose the standing-wave biperiodic on-axis coupled structure, operated on $\pi/2$ mode at 9.3 GHz. The RF focusing is introduced with noses in accelerating cells, and the external solenoid is unnecessary. The narrow energy spread has been achieved with a thermal DC gun and specially optimized bunching cells. The basic components of this linear accelerator are shown in **Fig. 1**. It consists of an RF power source, circulator, accelerating structure, thermal DC gun and titanium window. And **Table 1** presents some critical parameters of the accelerator.

This accelerator was designed, fabricated, low-power and high-power tested in our laboratory. The frequency of each cell, the distribution of on-axis electric field and coupling coefficient were measured during the cold test. The cold test results have shown a good agreement with our previous simulation. The high-power RF test has been carried out to measure the performance of this accelerator, including the output beam current, capture ratio, energy spectrum, the size of the beam spot, breakdown rate and other useful data.

This paper presents the RF design, simulation analysis, fabrication, and test results of this SW linear accelerator. The rest of this paper is organized as follows. In Section II, we illustrate the RF design and analysis of the X-band accelerating structure. The results of the calculation for electronic gun simulation and beam dynamics are also shown. Section III introduces the fabrication, tuning, and low-power RF test of the accelerating structure. In section IV, the setup and detailed results of the high-power RF experiment are presented. Finally, conclusion and outlook are made in Section V.

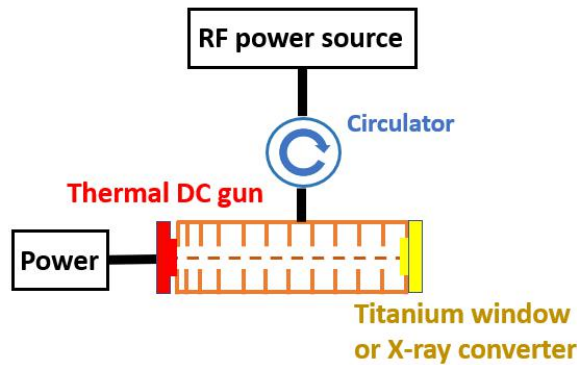


Fig. 1. Schematic diagram of the SW electron linear accelerator.

Table 1. Some basic parameters of this X-band SW linear accelerator.

Parameter	Value
Number of accelerating cavities	29
Length	0.59 m

Input RF power	2.4 MW
Pulse beam current	100 mA
Capture ratio	32%
RMS beam spot radius	0.5 mm
Energy dispersion	250 keV
Average accelerating gradient	15 MeV/m

II. RF design and analysis

A high accelerating gradient is necessary to improve the accelerating efficiency and increase the output beam energy without excessive length. The longitudinal shunt impedance of the accelerator is expected to be as large as possible within a reasonable range of the RF breakdown rate (BDR). We aim to find a group of appropriate structural parameters to satisfy these requirements simultaneously. In our design process, we implement cavity geometry optimization by SUPERFISH, beam dynamics study by ASTRA and full-scale RF simulations by CST codes [11-12].

A. Cavity geometry optimization

The geometric optimization of normal cells is essential to acquire high accelerating efficiency. In a linear accelerator, the kinetic energy that an electron gains can be considered as [13]:

$$W = \sqrt{Z_{eff} PL}, \quad (2)$$

where Z_{eff} refers to the effective shunt impedance, P is the microwave power loss, L refers to the longitudinal length.

With an increased Z_{eff} , this accelerator is shortened longitudinally. In the process of cavity geometry optimization, we aim to acquire a maximum longitudinal shunt impedance. **Fig. 2** shows the two-dimensional model we used for the geometry optimization. It can generate an axisymmetric structure based on two-dimensional models, and then calculate relative RF characteristic parameters. This method can reduce optimization time significantly, and hence greatly improve efficiency. Reduced coupling cell length and disk thickness will lead to a dramatically improved effective shunt impedance, but cavities will easily deform in processing. The beam pipe radius and nose radius are also critical to the longitudinal shunt impedance. However, a small beam pipe radius and nose radius will result in low capture coefficient because more bunches collide onto the beam pipe. Moreover, small nose radius will generate high BDR and the stability of the accelerator will be weakened. These parameters are therefore determined with proper values.

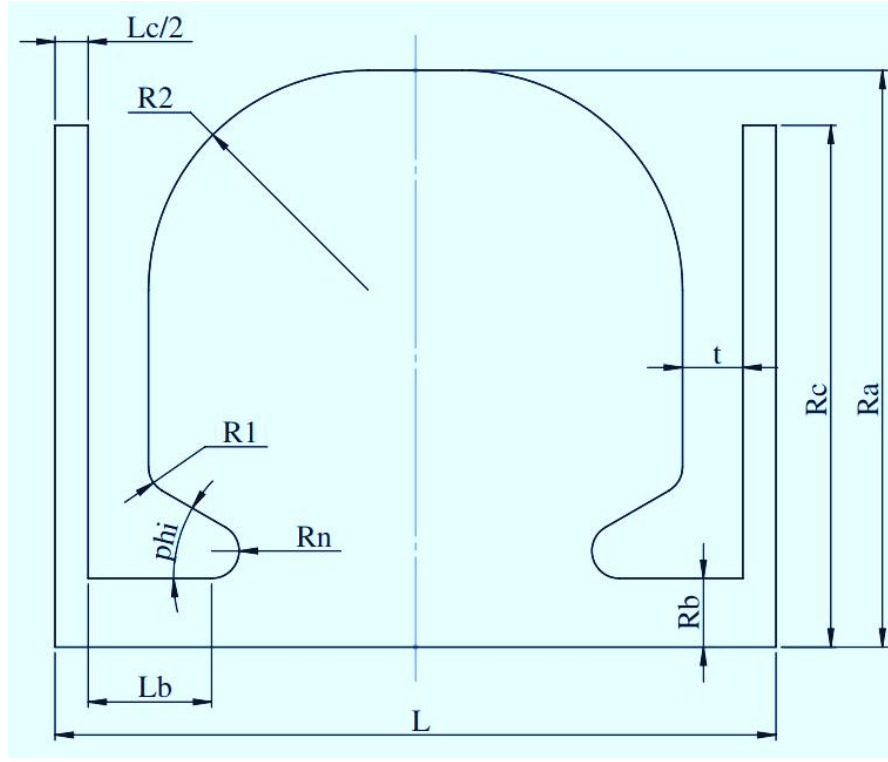


Fig.2. A two-dimensional model of a normal cell consisting of an accelerating cavity and a coupling cavity.

We chose $\pi/2$ mode as the work mode of the electron linear accelerator, for maximal adjacent mode separation and frequency robustness under operation. According to the bi-periodic structure theory, to maximize longitudinal shunt impedance, the coupling cell has a small volume and a very weak electromagnetic field inside it. In our model, the coupling cells have only 1.5 mm length longitudinally, so their effective shunt impedance and quality factor can be ignored.

The RF characteristics of the normal cell are presented in **Table 2**. The f_a indicates the frequency of accelerating cells, and the f_c represents the frequency of coupling cells. Z_{eff} is the effective longitudinal shunt impedance, and Q_0 implies the unloaded quality factor.

Table 2. RF characteristics of optimized accelerating and coupling cavities

Parameters	Values
f_a	9.3 GHz
f_c	9.3 GHz
Z_{eff}	165 M Ω /m
Q_0	8900

B. Design and simulation of the cavity chain

The nose makes the electric coupling through the beam hole rather weak. Hence magnetic coupling has been used instead. We have implemented magnetic coupling slots between accelerating cells and coupling cells, as shown in **Fig. 3**.

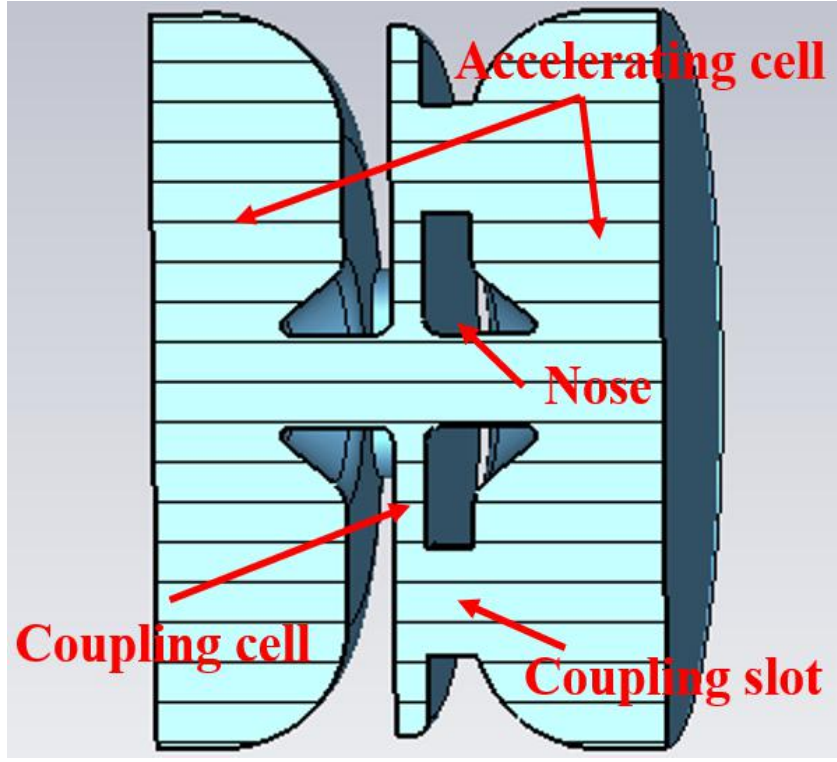


Fig. 3. Vacuum model of one normal cell, consisting of an accelerating and coupling cell.

First of all, the coupling coefficient between cavities was determined. In order to avoid the sub-adjacent coupling effect, the adjacent magnetic coupling slots were arranged orthogonally, as shown in **Fig. 3**. The dispersion equation for coupled cavity chain can be expressed [13]:

$$f_{\varphi} = \frac{f_0}{\sqrt{1 + k \cos \varphi}}, \quad (3)$$

where k refers to the magnetic coupling coefficient between cavities, and φ is the phase shift between cavities. We have to consider the separation between adjacent modes of the dominant mode $\pi/2$, so as to provide enough bandwidth between $\pi/2$ mode and its adjacent modes. Meanwhile, large coupling coefficient k leads to loss of accelerating efficiency. The coupling coefficient should be 2-3%, providing enough band-width between $\pi/2$ mode and its adjacent modes [12]. According to our calculation, when k equals to 2.7%, an adjacent modes separation of 10 MHz can be obtained. For bunching cavities, the stored power is inversely proportional to its magnetic coupling coefficient [15]. For bunching cells, we have pre-designed a unique on-axis electric field distribution that had to be formed by modifying the coupling coefficient between bunching cells to obtain a high capture rate as far as feasible. The procedure is the same as the one for normal cells described above.

C. Design of the external coupler and waveguide window

To feed RF power into the accelerator, an external coupler, consisting of a unique coupler cell and an external coupling hole, is connected to the rectangular waveguide. The vacuum model of the accelerator with a coupler is built in CST, as shown in **Fig. 4**. The results, including on-axis electric field distribution and S11, are displayed in **Fig. 5**.

The external coupling coefficient is expressed by [13]:

$$\beta = \frac{Q_0}{Q_e}, \quad (4)$$

where Q_0 is the unloaded quality factor of the accelerating structure, and Q_e refers to its external quality factor. If the beam current is very weak, the optimal external coupling coefficient is 1. However, if the beam loading is non-negligible,

the optimum external coupling coefficient should be calculated by [13]:

$$\beta_{opt} = \left(\frac{I}{2} \sqrt{\frac{ZL}{P_0}} + \sqrt{1 + \frac{I^2 ZL}{4P_0}} \right)^2, \quad (5)$$

Where I is the output beam current, P_0 is the input power, Z and L are the effective longitudinal shunt impedance and the length of accelerator respectively. According to our design, the output beam current is about 100 mA, the average energy is around 9 MeV, and the input RF power is 2.4 MW. In consequence, the optimum external coupling is about 1.96.

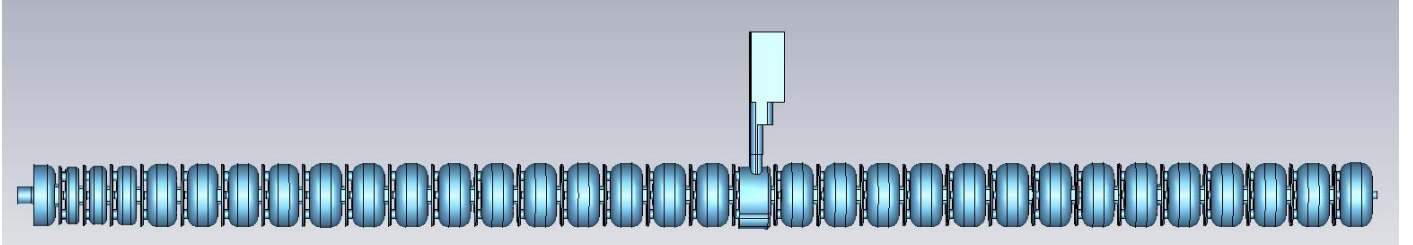


Figure 4. Vacuum model of the cavity chain, external coupler and waveguide for RF simulation in CST.

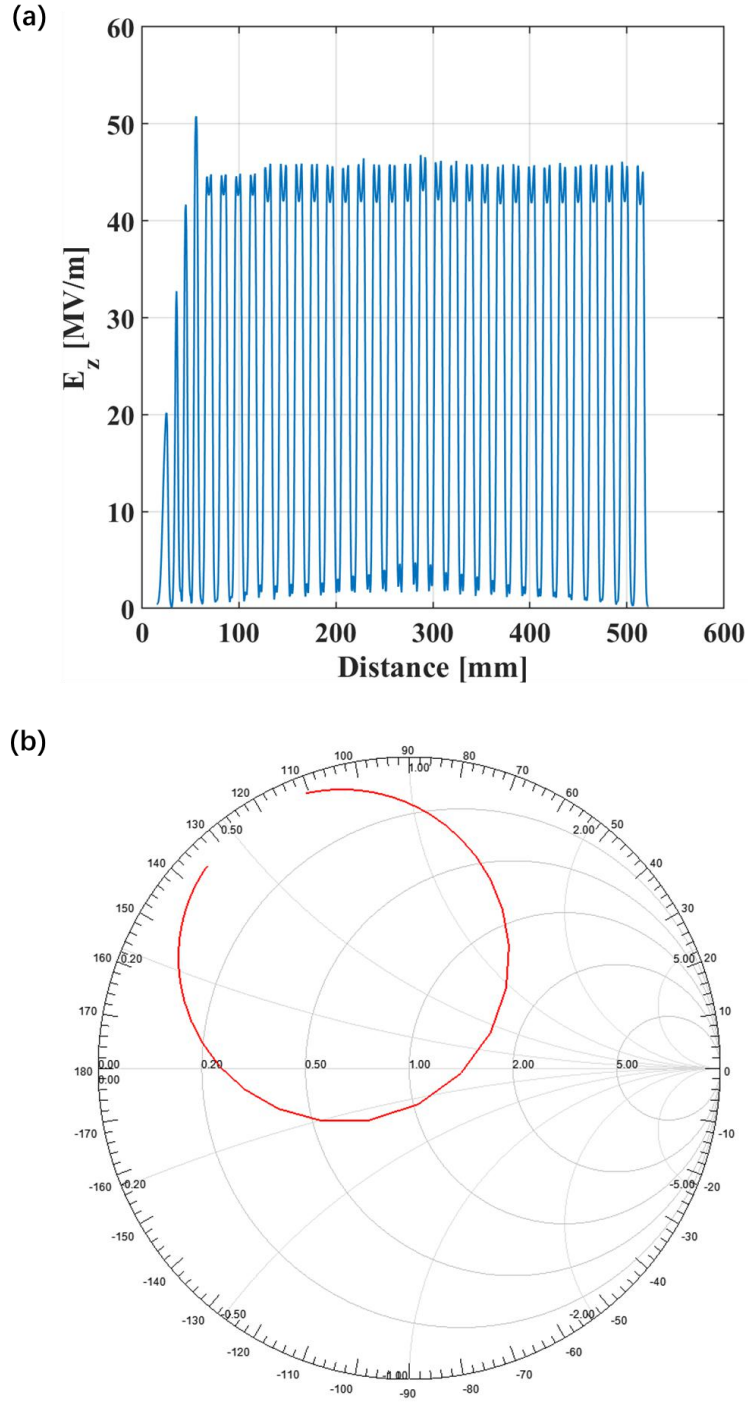
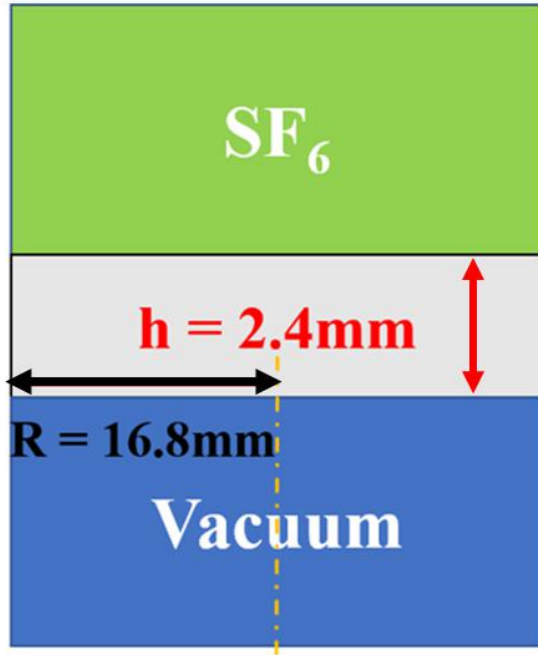


Fig. 5. (a) The magnitude of on-axis electric field of the accelerating structure. (b) The smith plot of the S_{11} parameter for the accelerating structure.

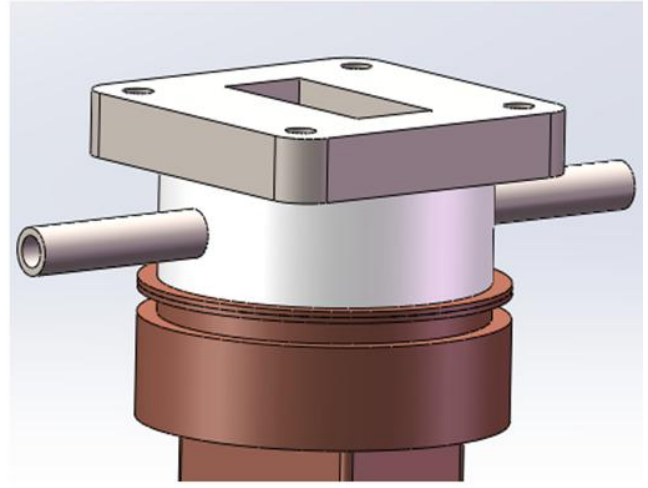
Waveguide windows are widely used in electric vacuum devices, for instance klystrons, magnetrons and accelerators. The waveguide window's function is to translate RF power with a low loss and to provide isolation between the vacuum within the accelerator and the SF6 inside the waveguide. In this accelerator, we optimized and fabricated a waveguide window based on a 2.4 mm-thick quartz dielectric slice, displayed in **Fig. 6**.

According to the classical transmission-line theory, when RF breakdown occurs in the accelerator, the terminal is mismatched and the incident wave is fully reflected. The transmission waveguide currently has some standing wave components. The RF window should be positioned distant from the standing wave's antinode and near the wave node, as indicated in **Fig. 7**, to reduce the probability of dielectric breakdown on the surface of the quartz window.

(a)



(b)



(c)

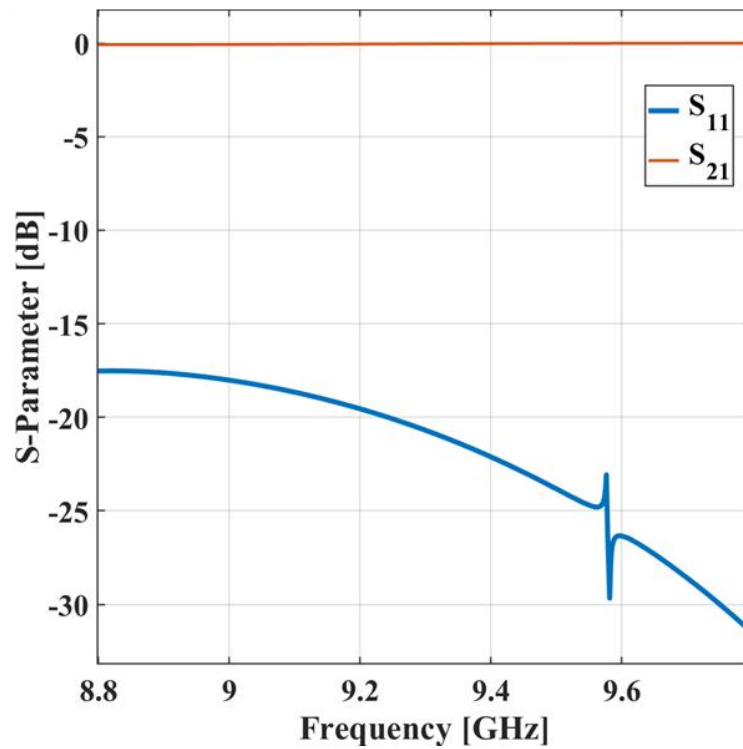


Fig. 6. (a) Components of the waveguide window system: SF_6 (green section) in the waveguide close to the power source, high vacuum (blue section) in the external coupler, and separated by quartz slice (gray section). (b) Mechanical design of the waveguide window, including the copper connector, the cooling water pipe, and the BJ84 rectangular flange. (c) S parameter plots of this waveguide window, of which blue line represents the S_{11} and orange line is S_{21} . The S_{11} is lower than -20dB at 9.3 GHz, demonstrating the feasibility of our waveguide window design.

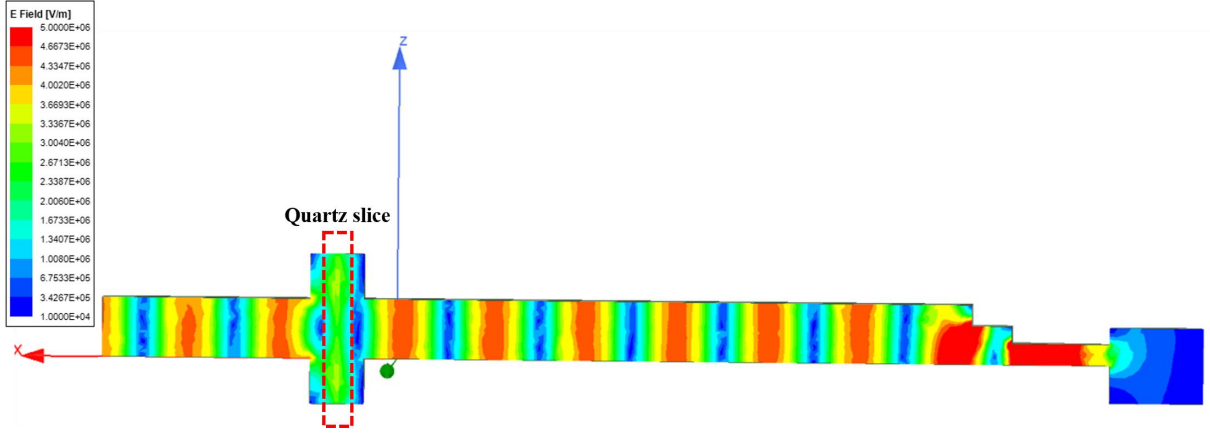


Fig. 7. Magnitude of the standing wave electric field inside the waveguide and coupler, when RF breakdown occurs in the accelerator and the input RF power is fully reflected.

D. Accelerating electric field built-up time

The field built-up time of RF structure is closely related to its loaded quality factor. The unloaded quality factor Q_0 of the cavity chain is obtained by CST simulation. The loaded quality factor can be directly calculated by unloaded quality factor Q_0 and external coupling coefficient β .

$$Q_L = \frac{Q_0}{1 + \beta}, \quad (6)$$

Based on the results of the RF analysis before, we can directly calculate that the Q_L is approximately 3055. In the process of field construction inside the accelerator, basic parameters such as the electromagnetic field and input impedance inside the structure change exponentially. The amplitude of the electric field in the cavity increases exponentially with time:

$$\frac{E}{E_{steady}} = 1 - e^{-\frac{\omega_0 t}{2Q_L}} = 1 - e^{-\frac{t}{t_F}} \quad (7)$$

We have calculated that at the end of transient time $4 \cdot t_F$, the magnitude of the electromagnetic field reaches about 98%, compared with the steady state. During the electromagnetic field construction, the field distribution is time-varying, reaching 9.0 MeV at the steady state. And according to theoretical calculation, there exists an optimal injection time t_{opt} that makes the injected electron beam accelerate to 9.0 MeV stably at and after this time [14]:

$$t_{opt} = \left(\ln \frac{I}{2} \sqrt{\frac{\beta_e P_0}{Z T^2 L}} \right) t_F \quad (8)$$

We can obtain that $t_{opt} \approx 2.46 \cdot t_F$. Compared with the 10 μ s microwave macro pulse width, the transient field built-up time is only 0.27 μ s, and can be ignored.

III. Simulation of the thermal DC gun and beam dynamics

A. Thermal DC gun

We adopted a thermal-cathode DC gun as the electron source, whose components mainly include the cathode, heating filament, focusing electrode, anode, insulating ceramic shell, and connector to the accelerator. The emission model was

simulated in the CST particle module. The emission current at 12.5 kV high voltage is 320 mA, and the perveance is 0.23 μ P. The simulation results and basic parameters are shown in **Fig. 8**, and the basic parameters of the DC gun are listed in **Table 3**.

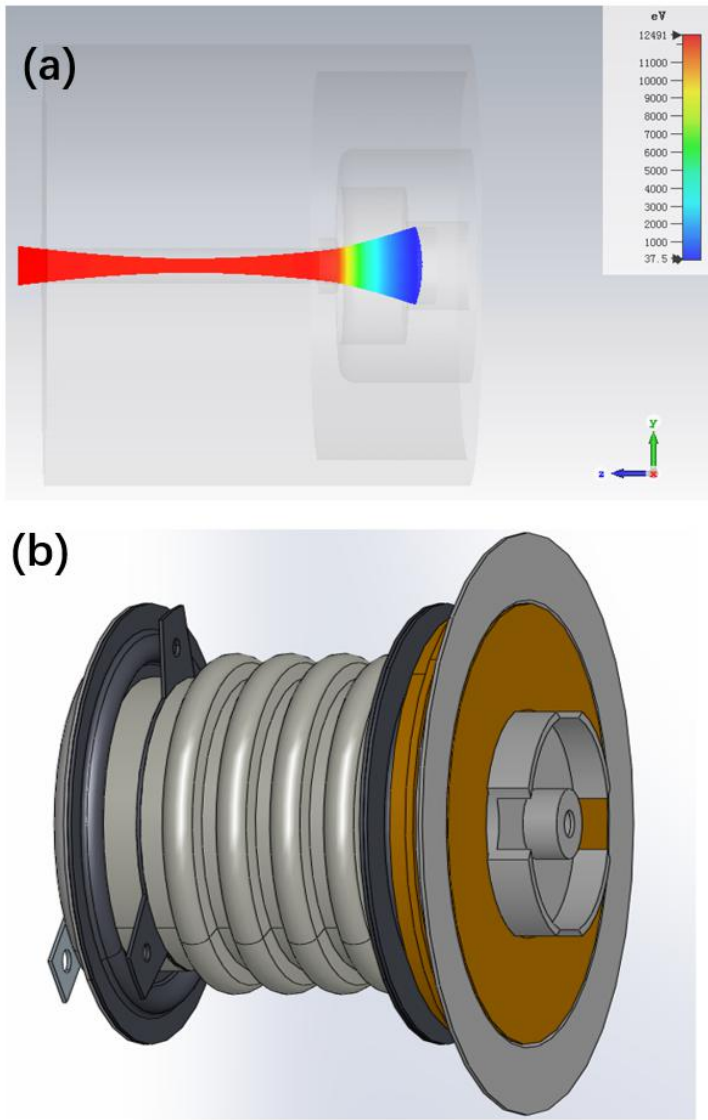


Figure. 8. (a) Beam simulation of the thermal DC gun at CST. (b) Mechanical design of the thermal DC gun.

Table 3. Parameters of the thermal-cathode DC gun. In the table, V_e refers to the high voltage applied between cathode and anode, I_e is the emission current, P_e indicates the perveance of our electronic gun, R_w is the RMS radius at beam waist, L_w is the distance between the beam waist and cathode, and R_h is the beam pipe radius.

Parameter	Value
V_e	12.5 kV
I_e	320 mA

P_e	0.23 μP
R_w	0.316 mm
L_w	13.05 mm
R_h	1.5mm

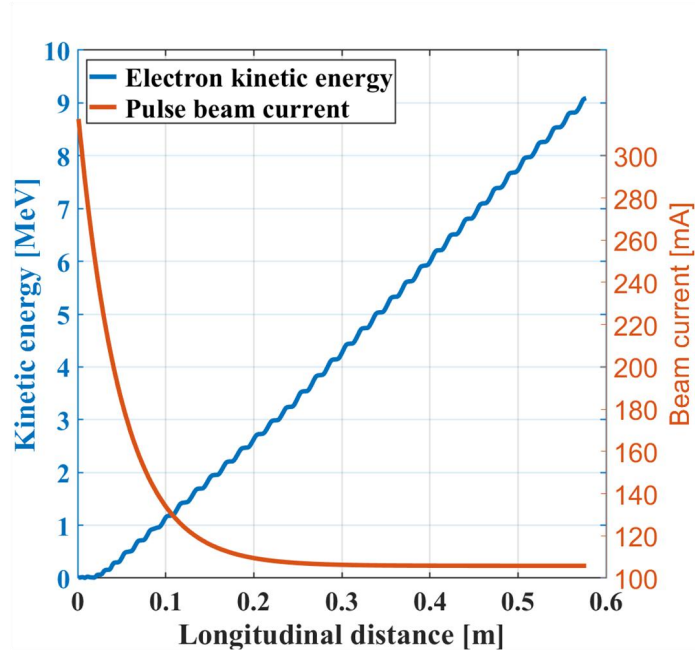
B. Beam dynamics study

Our design process carried out a beam dynamics study through ASTRA codes. The apertures were carefully set up based on the position of the noses and their radius. We can match the real accelerating structure and achieve accurate beam loss calculation. A 100 mA pulse beam current and a capture ratio of 32% were achieved. More results of the beam dynamics calculation are shown in **Fig. 9**.

The accelerating structure noses generate a weak RF focusing/defocusing for the electron beams during their transit. Depending on the electric field distribution of a symmetric accelerating cell, the electron will be focused and defocused alternately. However, their momentum is greater when electrons are focused than when they are defocused, leading to an overall focusing effect.

Along the light-speed section, the energy of accelerating electrons gradually increases, and the space charge force decreases. Benefiting from the RF focusing effect, additional solenoid is unnecessary to be applied in our design, to reduce the extra space cost and inconvenience. **Fig. 10** exhibits the beam spot, the transverse and longitudinal phase space distributions at the exit of the accelerator.

(a)



(b)

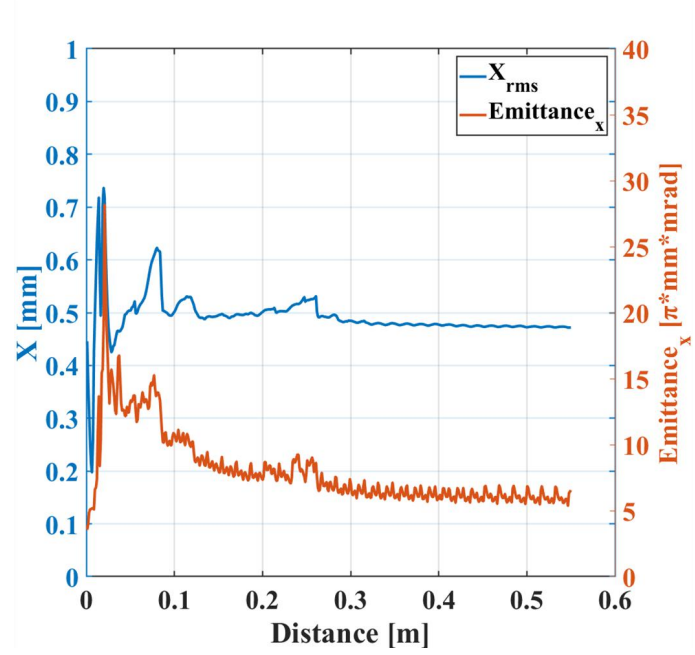


Fig. 9. Statistical results of the beam dynamics simulation. (a) The kinetic energy (blue line) and the pulse beam current (orange line) along the accelerating structure longitudinally. (b) The RMS beam spot radius (blue line) and the transverse beam emittance (orange line) along the accelerating structure longitudinally.

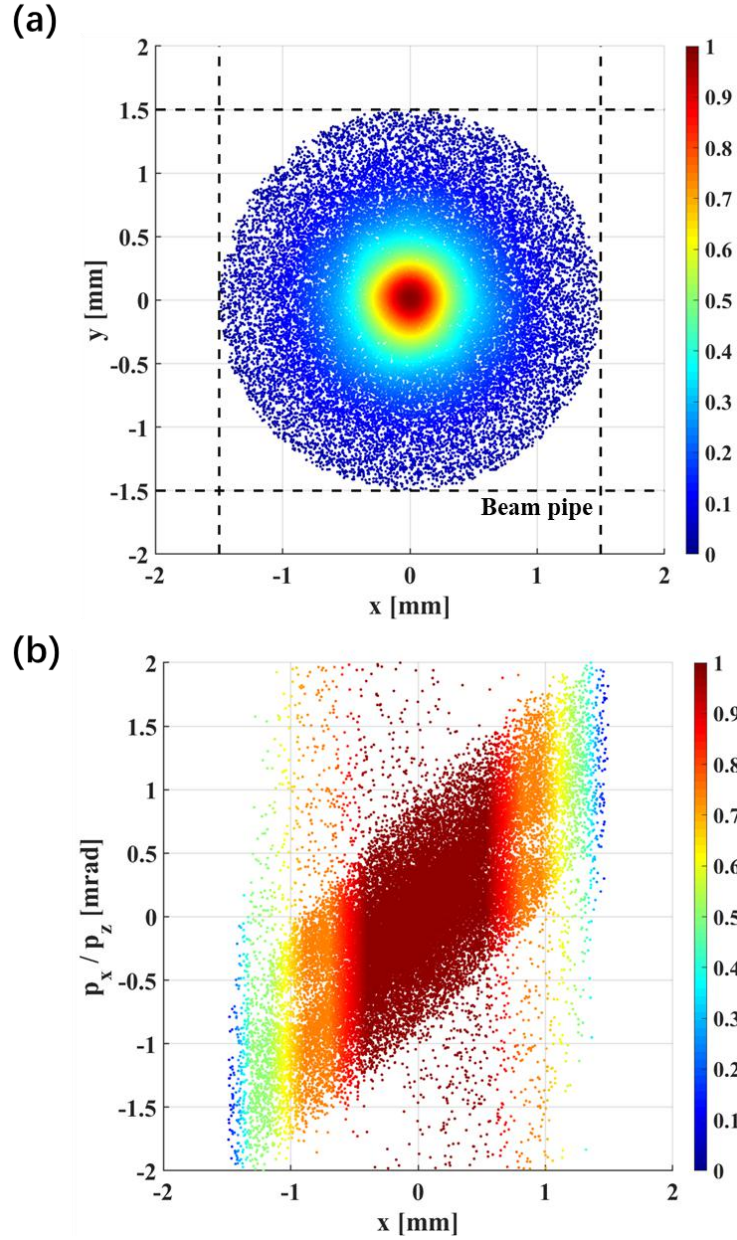


Fig. 10. Beam information at the exit of the accelerator, for 10^5 macro particles during the beam dynamics calculation. (a) Transverse beam spot (the dash line is the beam pipe radius of 1.5 mm). (b) Transverse phase space.

IV. Low-power RF test

There were 33 pairs of disks manufactured in total. Four cooling water channels were processed on the copper disks. Due to the thin thickness, all copper disks were fabricated without tuning holes or pins. Each disk has been processed with a smaller cavity radius. After each cold test, unsatisfying copper disks, were reprocessed on the high-precision milling machine. The structure is reprocessed for cavities with a large deviation away from 9.3 GHz to achieve fine-tuning. All RF cavities were tuned into an appropriate range around the operating frequency of (9300 ± 5) MHz. RF cold test was carried out at each step of the fabrication. The test results of the last machining round agreed well with the simulation results.

Some disks and the low-power RF test setup are displayed in **Fig. 11**. We assembled the cavity chain with fixture, measured the on-axis field distribution with the bead-pull method, and sampled the S_{11} data [15-18]. We also compared it with our previous simulation results, as shown in **Fig. 12**. The measured on-axis field distribution can be compared with **Fig. 5 (a)**. The cold test results showed a good agreement between the simulation and actual measurement.

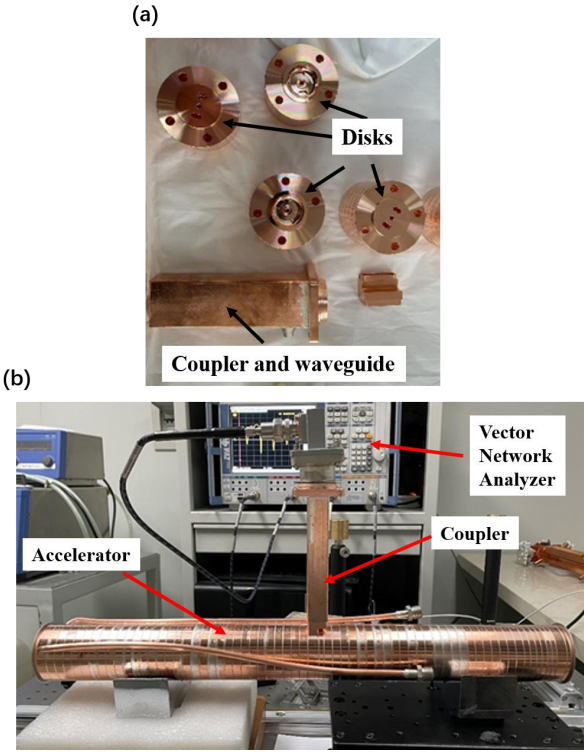


Fig. 11. (a) Copper disks, coupler waveguide and waveguide after fabrication. (b) A picture of the low-power RF test setup.

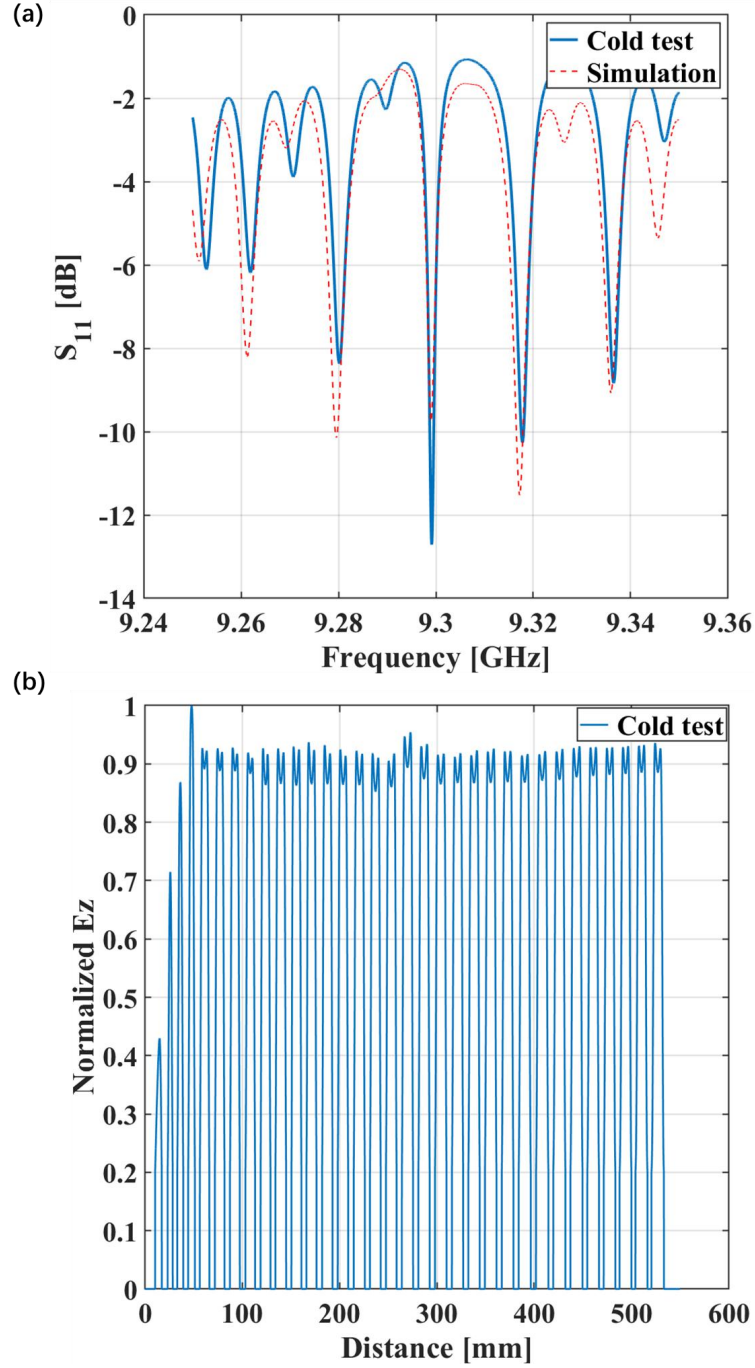


Fig. 12. Low-power RF measurement results of the accelerator. (a) The magnitude of the S_{11} parameter: the red dashed line is the S-parameter of the simulation result, and the blue line is the cold test result. (b) The relative magnitude of the on-axis electric field in the cold test.

V. High-power RF experiment

A. High-power experiment platform and conditioning

A silver-based alloy brazed the assembled cavity chain, waveguide coupler, and quartz waveguide window. Then the cooling water pipe, thermal DC gun and the titanium window were welded to the accelerator structure with an argon arc. After vacuum-leak detection and cathode activation of the thermal DC gun, a complete accelerator was obtained, as shown in Fig. 13.

Through the waveguide and titanium windows, the vacuum inside the accelerator tube is sealed, so as to be isolated from SF₆ gas in the high-power waveguide transmission system. A CF63 flange was installed to connect with the magnetic

spectrometer and measure the output beam's energy spectrum. A titanium getter pump is welded on the waveguide to maintain a low vacuum degree of the accelerating structure. The vacuum degree of the accelerating structure is kept to be lower than 10^{-6} Pa. With the fixed perveance of the thermal DC gun, we can change the emission current by adjusting the high voltage applied on it. The emission and pulse beam currents rise when the high voltage is enhanced. The mismatch between the initial kinetic energy and the accelerating field will cause a drop in the capture ratio at excessive voltages (>13 kV). We adjusted the high voltage in the 12–13 kV range for the high-power experiment.

For this completed accelerator, RF characteristics were measured. The reflection coefficient, standing wave ratio, quality factor, and external coupling coefficient were also calculated. The measuring instrument is an R&S ZVA60 Vector Network Analyzer. No significant frequency shift was observed after brazing. The simulation results are slightly higher than the external coupling coefficient of 1.8. The reason may be the error of waveguide port calibration before the cold test, and the unsatisfactory electrical contact between the waveguide window and the measurement port.

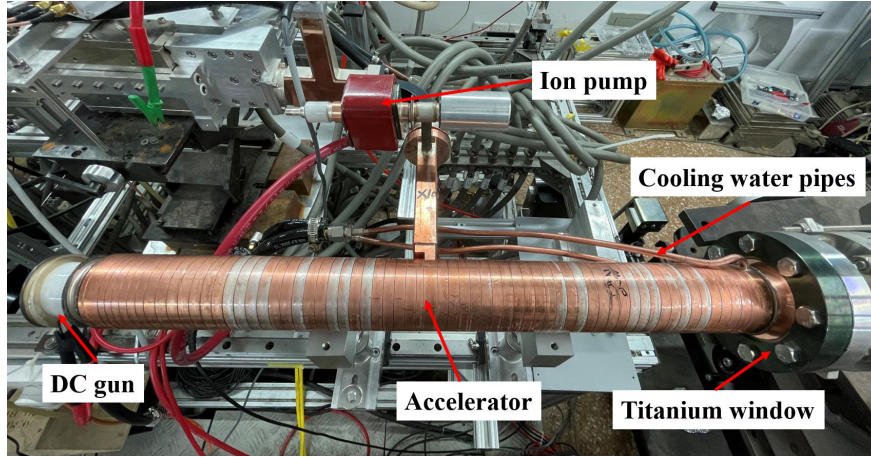


Fig. 13. The whole accelerator with all components, including the thermal DC gun, titanium window, cooling pipes and ion pump.

Based on the study of the RF breakdown phenomenon of high-gradient accelerating structure, we know that the RF breakdown rate (BDR) is closely related to the accelerating gradient and the RF pulse width. The relationship between BDR and accelerating gradient as well as pulse width can be expressed as [19-21]:

$$\frac{BDR}{E_{acc}^{30} t_p^5} = const \quad (9)$$

In our high-power experiment, the klystron pulse is long, up to $10 \mu s$, and the ignition rate is high. It must be conditioned in advance to reduce BDR and improve stability during the high-power experiment. The RF power fed into the accelerator was gradually increased and we kept the BDR below 10^{-4} /pulse all the time, to avoid irreversible damage to the cavity wall. The accelerating structure was fully conditioned to control the BDR below 10^{-4} /pulse [22-23], with 2.4 MW input RF power.

We built a high-power experimental platform to obtain this accelerator's high-power results. A compact 2.4 MW X-band high-power multi-beam klystron was installed as the RF power source, to provide input RF power for the accelerator. The circulator separates the klystron and accelerator and these components are connected together by waveguide filled with high-pressure SF_6 gas. To monitor the incident wave into the accelerator and the reflected wave from the accelerator, we installed several directional couplers. Besides, to measure the output beam current, we installed a Faraday cup with an integrated circuit at the accelerator's exit.

We have used a Tektronix DPO4034 oscilloscope to sample electrical signals, including: the klystron's emitting current and collector current of the thermal DC gun, emission current and high voltage, and the output beam current collected by the Faraday cup. Moreover, de-noising processing was done on electrical signals to eliminate the high-voltage interference from the high-voltage modulator. We used a Rode & Schwarz NRP-Z81 power meter for microwave signals to measure the accelerator's incident wave and reflected wave signals. The beam current waveform, the energy spectrum, the capture

coefficient, and the output beam spot size were measured and evaluated during the high-power experiment.

B. Results of the high-power experiment

Signals of the output beam current and high voltage applied on the thermal DC gun, were sampled by the Tektronix DPO4034 oscilloscope. We have displayed the best data in **Fig. 14**, of which the pulse width is $9.8\mu\text{s}$, the pulse beam current is 100 mA, and the repetition rate is 50 Hz (i.e. the operating duty ratio is 0.5%). Due to some mismatch between the klystron and the modulator, the input RF power is not strictly flat, and decreases slowly along the pulse time. And this imperfect input RF pulse causes a slight decline in the waveform of the output beam current. We have taken the ratio between the output beam current and emission current from the thermal DC gun, as an estimation of the capture ratio approximately. Under conditions in **Fig. 14**, we measured and calculated the capture ratio of $(31.2 \pm 0.5)\%$. This capture ratio is just below the predicted result of 32%, possibly due to processing and measurement errors.

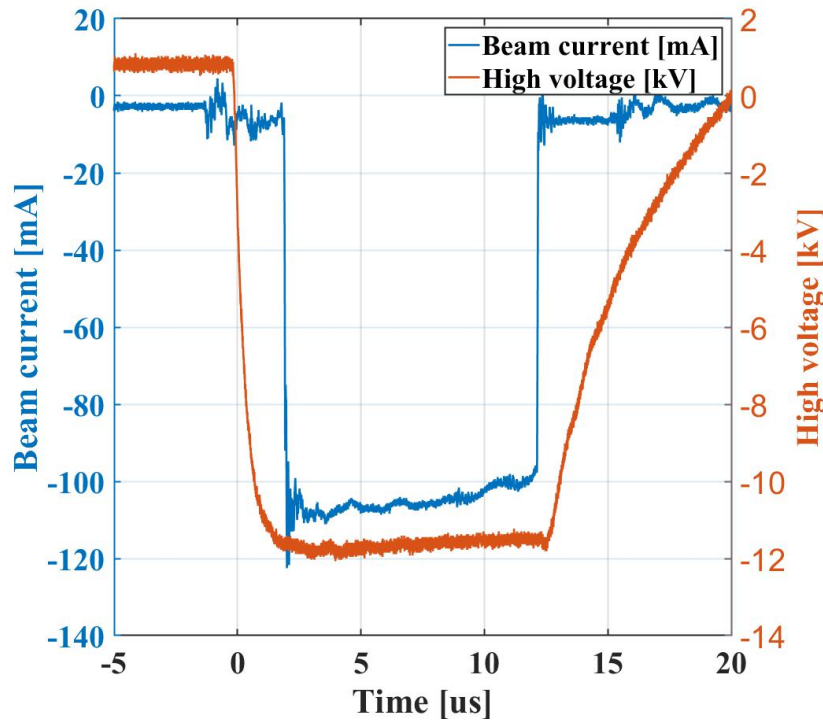
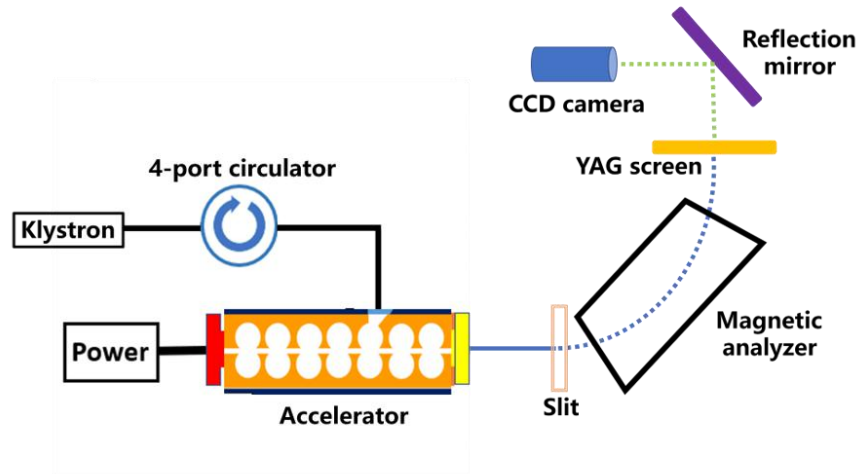


Fig. 14. The signals of the output beam current and high voltage applied on the thermal DC gun.

A magnetic spectrometer was installed at the exit of the linear accelerator, which is shown in **Fig. 15**, to measure the beam energy spread. To reduce the beam spot size and improve the energy resolution, a slit with dimensions of 38 mm in length and 0.2 mm in width was inserted at the magnetic spectrometer's entry during the test. The size of the slit affected the relative brightness significantly on the screen, to greatly impact on the energy resolution. Through adjusting the magnetic field, electrons with different kinetic energy will have its unique drifting trajectory. According to the position and brightness on the YAG screen, we can evaluate the beam energy spread. The energy spectrums of the output beam corresponding to different input power are shown in **Fig. 16**. For 2.4 MW input power, the kinetic energy of output beam is 9.04 MeV and the FWHM of the energy spectrum is about 3.5%.

(a)



(b)

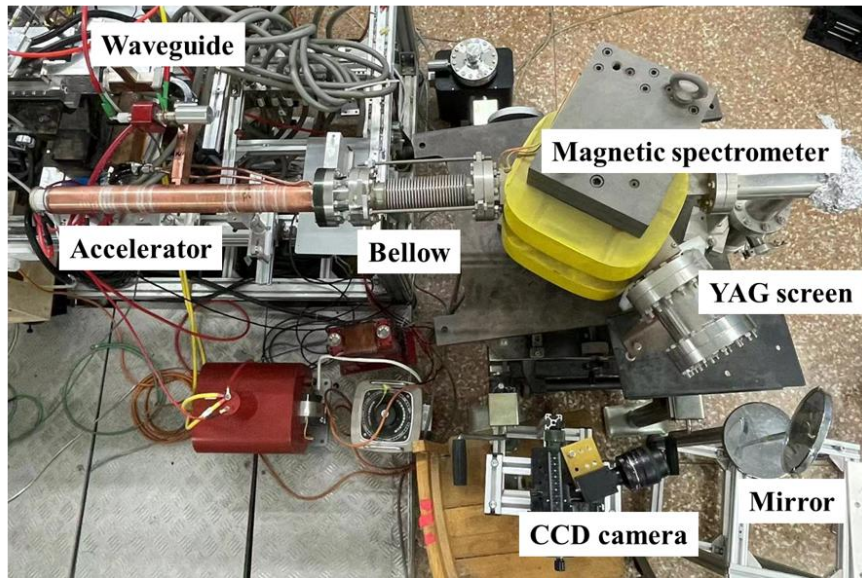


Fig. 15. (a) The energy spread measurement experiment schematic diagram. (b) Image of the energy spread measurement setup inside the shielding room.

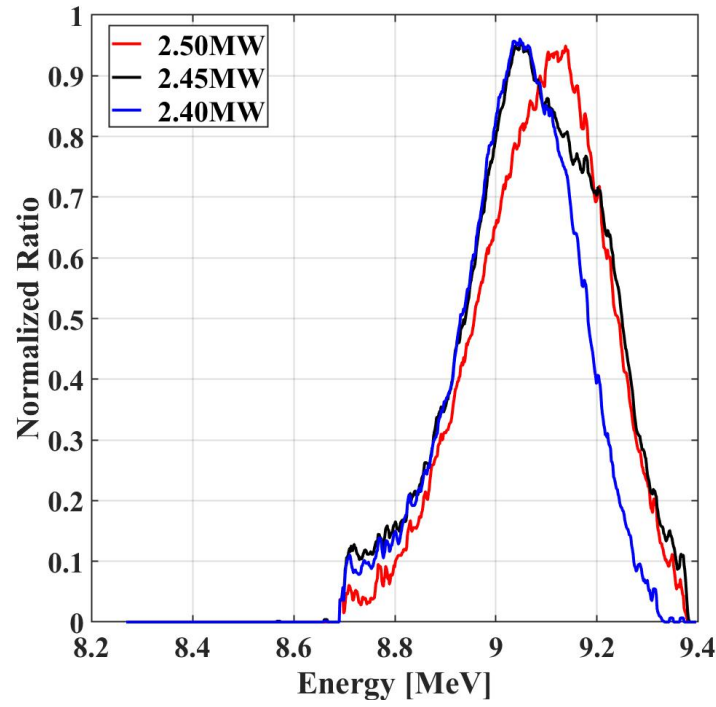


Fig. 16. Energy spread measurement results with different input RF power applied.

A mirror placed with 45 degrees acute-angle to the beam line, reflected light from the YAG screen. A CCD camera with a focusing lens was applied to capture the image. The CCD camera had a resolution of about 50 m/pixel. The spot size of output beam was estimate by the picture on the YAG screen. The brightness distribution of the images may be used to determine the RMS diameter of the beam since the brightness of optical transition radiation was proportional to the number of incoming particles. For 2.4 MW input RF power and 100 mA pulse beam current, the beam spot image was captured by the CCD camera and the calculated RMS radius of the RMS beam spot was about 0.5 mm, as shown in **Fig.17**.

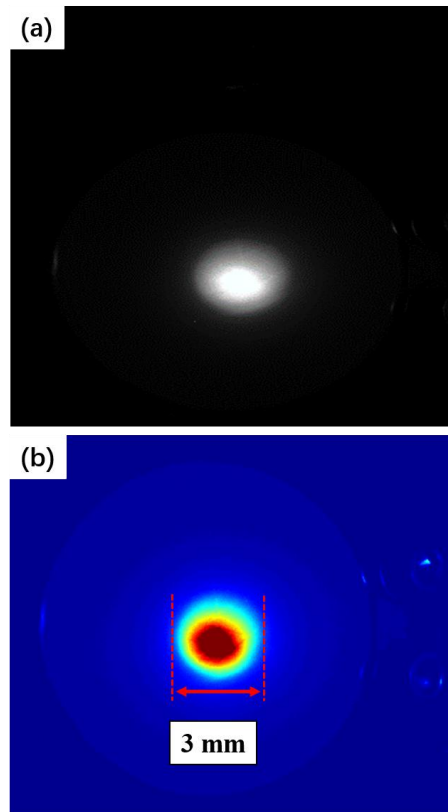


Fig. 17. (a) Beam spot photo captured by the CCD camera. (b) Brightness analysis result in post-processing.

Conclusion

An X-band 9 MeV SW linear accelerator powered by a 2.4 MW klystron has been developed at Tsinghua University. Its advantages includes RF focusing without solenoid, low energy spread with a thermal DC gun, and no tuning pins.

During the design process, employing SUPERFISH, CST and ASTRA codes, it is easy to complete the pre-design of accelerator RF parameter design, cavity geometry optimization, cavity chain RF simulation, and the beam dynamics study. We conducted a low-power RF test after fabricating and tuning each copper disk. The results of the cold test and the simulation results were in good accord.

A high-power RF experiment was carried out on the accelerator. During the high-power test, we measured the output beam current, capture ratio, beam energy spectrum, and the beam spot size at the exit of this linear accelerator. With 2.4 MW input RF power, we obtained 100 mA beam current and about 9.8 μ s pulse width (under 0.1% duty factor). The output RMS spot radius was 0.5mm around, and the output kinetic energy was 9.04 MeV, with a 3.5% FWHM spectrum width. Results of the high-power RF experiment showed good performance of this accelerator. We will examine its performance in the future with a high duty factor of 1%. Further explorations will also be carried out on this linear accelerator for higher-order modes.

Acknowledgments

This work is supported by key R&D project of the Ministry of Science and Technology of China (Grant No. 2022YFC2402300).

References

1. C.X. Tang, Present status of the accelerator industry in Asia, in *Proceedings of the 1st International Particle Accelerator Conference, Kyoto, Japan* (2010)
2. E. Tanabe, A. Associates, Medical application of C-band accelerator technologies, in *Proceedings of the 19th International Linear Accelerator Conference, Chicago, USA* (1998)
3. C.X. Tang, H.B. Chen, Y. Liu et al., Low-energy linacs and their applications in Tsinghua university, in *Proceedings of the 23rd International Linear Accelerator Conference, Knoxville, USA* (2006)
4. Y. Kamino, S. Miura, M. Kokubo et al., Development of a new concept automatic frequency controller for an ultra-small C-band linear accelerator guide, *Med. Phys.* **34**, 1797 (2007). doi: [10.1118/1.2752581](https://doi.org/10.1118/1.2752581)
5. X.C. Lin, H. Zha, J.R. Shi et al., Fabrication, tuning, and high-gradient testing of an X-band traveling-wave accelerating structure for VIGAS, *Nucl. Sci. Tech.* **33**, 102 (2022). doi: [10.1007/s41365-022-01086-y](https://doi.org/10.1007/s41365-022-01086-y)
6. J.H. Shao, H.B. Chen, Q.Z. Xing, Design of a C-band 6 MeV standing-wave linear accelerator structure, in *Proceedings of the 2nd International Particle Accelerator Conference, San Sebastian, Spain* (2011)
7. J.H. Shao, H. Zha, H.B. Chen, Fabrication and high power RF test of a C-band 6 MeV standing-wave linear accelerating structure, in *Proceedings of the 3rd International Particle Accelerator Conference, New Orleans, LA, USA* (2012)
8. J.H. Shao, H. Zha, H.B. Chen et al., High power test of a C-band 6 MeV standing-wave linear accelerator, in *Proceedings of the 4th International Particle Accelerator Conference, Shanghai, China* (2013)
9. J.H. Shao, Y.C. Du, H. Zha et al., Development of a C-band 6 MeV standing-wave linear accelerator, *Phys. Rev. Accel.*

Beams. **16**, 090102 (2013). doi: [10.1103/PhysRevSTAB.16.090102](https://doi.org/10.1103/PhysRevSTAB.16.090102)

10. C.M. Ma, S.B. Jiang, Monte Carlo modelling of electron beams from medical accelerators. *Phys. Med. Biol.* **44**, 157 (1999). doi: [10.1088/0031-9155/44/12/201](https://doi.org/10.1088/0031-9155/44/12/201)
11. <https://www.cst.com>
12. <https://www.desy.de/~mpyflo/>
13. J. Shi, Dissertation, Tsinghua University, 2009
14. T. P. Wangler, RF Linear accelerators, John Wiley & Sons, 2008
15. X.C. Lin, H. Zha, J.R. Shi et al., Development of a 7-cell S-band standing-wave RF-deflecting cavity for Tsinghua Thomson scattering X-ray source, *Nucl. Sci. Tech.* **32**, 36 (2021). doi: [10.1007/s41365-021-00871-5](https://doi.org/10.1007/s41365-021-00871-5)
16. X.C. Lin, H. Zha, J.R. Shi et al., Design, fabrication, and testing of low-group-velocity S-band traveling-wave accelerating structure, *Nucl. Sci. Tech.* **33**, 147 (2022). doi: [10.1007/s41365-022-01124-9](https://doi.org/10.1007/s41365-022-01124-9)
17. Shi J, A Grudiev, A Olyunin et al. Tuning of CLIC accelerating structure prototypes at CERN, in *Proceedings of the 28rd International Linear Accelerator Conference, Tsukuba, Japan* (2010)
18. J. Shi, A. Grudiev, W. Wuensch, Tuning of X-band traveling-wave accelerating structures, *Nucl. Instrum. Meth. A.* **704**, 14 (2013). doi: [10.1016/j.nima.2012.11.182](https://doi.org/10.1016/j.nima.2012.11.182)
19. M.M. Peng, J.R. Shi, H. Zha et al., Development and high-gradient test of a two-half accelerator structure, *Nucl. Sci. Tech.* **32**, 60 (2021). doi: [10.1007/s41365-021-00895-x](https://doi.org/10.1007/s41365-021-00895-x).
20. V. Dolgashev, Study of basic breakdown phenomena in high gradient vacuum structures, in *Proceedings of Linear Accelerator Conference, LINAC2010, Tsukuba, Japan* (2010)
21. V. Dolgashev, S. Tantawi, Y. Higashi et al. Geometric dependence of radio-frequency breakdown in normal conducting accelerating structures, *Appl. Phys. Lett.* **97**, 171501 (2010). doi: [10.1063/1.3505339](https://doi.org/10.1063/1.3505339)
22. A. Grudiev, W. Wuensch, S. Calatroni, New local field quantity describing the high gradient limit of accelerating structures, *Phys. Rev. Spec. Top-Ac.* **12**, 102001 (2009). doi: [10.1103/PhysRevSTAB.12.102001](https://doi.org/10.1103/PhysRevSTAB.12.102001)
23. A. Degiovanni, W. Wuensch, G.N. Jorge, Comparison of the conditioning of High Gradient Accelerating Structures, *Phys. Rev. Accel. Beams.* **19**, 032001 (2016). doi: [10.1103/PhysRevAccelBeams.19.032001](https://doi.org/10.1103/PhysRevAccelBeams.19.032001)